Post-print version (generated on 14.12.2023)
This and other publications are available at:
http://www.acin.tuwien.ac.at/publikationen/ams/

Reconstructing highly divergent wavefronts from sparse measurements

Nikolaus Berlakovich[1*], Ernst Csencsics[1], Damian Senoner[1], and Georg Schitter[1]

[1] *Automation and Control Institute (ACIN), TU Wien, 1040 Vienna, Austria*
[*] *Corresponding author: berlakovich@acin.tuwien.ac.at*

Compiled December 14, 2023

The paper presents a concept for the sparse measurement and reconstruction of highly divergent wavefronts enabling measurements at high throughputs and beyond the dynamic range of the wavefront sensor. In the proposed concept, a direct measurement of the wavefront is carried out, where a few segments of the wavefront are measured with Shack-Hartmann sensors (SHSs). In total about 1 % of the wavefront is measured and used for the reconstruction of the entire wavefront which makes the concept suitable for applications where low measurement times are needed. A simulation analysis and an experimental validation of the concept are carried out and results show that a wavefront with a divergence of 62° can be reconstructed with a root-mean-square error of about 200 nm.
© 2023 Optical Society of America

OCIS codes: (150.1135) Algorithms; (120.3940) Metrology; (120.5050) Phase measurement; (220.4840) Testing; (280.4788) Optical sensing and sensors.

http://dx.doi.org/10.1364/ao.XX.XXXXXX

1. INTRODUCTION

The Shack-Hartmann sensor (SHS) is frequently used in adaptive optics [1, 2] and for the assessment of optical systems [3], owing to its compactness, insensitivity to vibrations, and reference-free measurement once the sensor is calibrated, e.g. with a plane wavefront [4, 5]. Highly divergent wavefronts cannot be measured directly with a single SHS, as they typically exceed the dynamic range of the sensor [6]. Supporting optics, such as null optics, may be used to transform the wavefront into a wavefront within the dynamic range. One drawback of supporting optics is that they may introduce additional errors in the measurement [6]. In [7–9] a concept is proposed, enabling the measurement of a highly divergent wavefront without supporting optics. In particular, the sensor is mounted on a positioning system that moves the sensor to perform partially overlapping measurements of the wavefront. The registration of the measurements by minimizing the overlap mismatch leads to the reconstruction of the entire wavefront [10–14]. The registration can be carried out at a time scale of sub-seconds but the large number of measurements (>100) required to cover the entire wavefront leads to measurement times at the scale of minutes making the concept unsuitable for time-critical applications, such as inline metrology.

The contribution of this paper is a concept for the sparse measurement and reconstruction of highly divergent wavefronts based on a modal approach. Inspired by a concept for the fast acquisition of plane wavefronts with large diameters [15], a small fraction of the wavefront is directly measured using several SHSs. Section 2 introduces the concept. Section 3 presents a simulation analysis of the concept and Section 4 presents an experimental validation of the concept. Section 5 concludes the paper.

2. CONCEPT

A. Wavefront measurement

A sparse measurement of the divergent wavefront is carried out where only few segments of the wavefront are measured using SHSs. Each sensor has a specific position measuring a specific segment of the wavefront, i.e. a wavefront segment, as illustrated in Fig. 1a. Owing to the sparsity of the measurement, there are no overlaps between the sensors enabling a parallel acquisition of the measurements.
An experimental setup with 5 SHSs is illustrated in Fig. 1b, where about 1 % of the total wavefront is measured. The wavefront with a divergence of 62° originates from an optical fiber and is measured at a radius of 90 mm. The aperture of each sensor is approximately orthogonal to the direction of propagation of the incident wavefront to enable a measurement within the dynamic range of the sensor. By propagating through a micro-

Post-print version of the article: Nikolaus Berlakovich, Ernst Csencsics, Damian Senoner, and Georg Schitter , “Fast modal reconstruction of large plane wavefronts from sparse measurements using Shack–Hartmann sensors,” *Applied Optics*, Vol. 62, Issue 26, pp. 6986-6992, 2023. DOI: 10.1364/AO.493076
© 2023 Optical Society of America. One print or electronic copy may be made for personal use only. Systematic reproduction and distribution, duplication of any material in this paper for a fee or for commercial purposes, or modifications of the content of this paper are prohibited.

Post-print version (generated on 14.12.2023)
This and other publications are available at:
http://www.acin.tuwien.ac.at/publikationen/ams/

scope slide, the wavefront is distorted, i.e. deviated from the spherical wavefront. The distortions are described by a linear combination of Zernike polynomials (ZP) with unknown coefficients [16]. Estimating the coefficients from the measurement data results in modal reconstruction of the wavefront.
In Section 4 details and results of the experimental setup are discussed.

B. Wavefront reconstruction

The used parameterization (θ_1, θ_2) of the wavefront in the global frame (FG) is given by

$$\boldsymbol{w} = \begin{pmatrix} w_1 = \tilde{r}\, sin(\theta_1)\, cos(\theta_2) \\ w_2 = \tilde{r}\, sin(\theta_1)\, sin(\theta_2) \\ w_3 = -\tilde{r}\, cos(\theta_1) \end{pmatrix}. \tag{1}$$

$$\text{with} \quad \tilde{r} = r_0 + \sum_{n=1}^{N} c_n\, Z_n(\theta_1, \theta_2),$$

where $\theta_1 \in [0, \theta_{div}]$, $\theta_2 \in [0, 2\pi]$ and $\boldsymbol{w}$ is the respective point belonging to the wavefront (see Fig. 2). The radius and the divergence of the nominal sphere of the wavefront are denoted by r_0 and $2\,\theta_{div}$, respectively. The deviations of the wavefront from the nominal sphere are described by a linear combination of Zernike polynomials (Z_n) [16] with unknown coefficients (c_n). The substitution of the first common argument of the Zernike polynomials, i.e. the radial distance in the x_1, x_2-plane, by θ_1 relates the polynomials to the sphere enabling better exploitation of the relationship between Zernike polynomials and wavefront aberrations.
The position and alignment of a sensor $u = 1..U$ is defined by two parameters, i.e. θ_{u1} and θ_{u2}, and the transformation of $\boldsymbol{w}$ from FG into the local coordinate system of the sensor, i.e. FSu, is given by

$$\boldsymbol{w}^{\{u\}} = R_{x_2}(\theta_{u1})\, R_{x_3}(-\theta_{u2})\, \boldsymbol{w} + (0, 0, r_0)^T, \tag{2}$$

with R_{x_2} and R_{x_3} being the rotation matrices about the x_1- and x_2-axis [17], respectively (see Fig. 2). The upper index in curly brackets $(\{u\})$ indicates the representation in FSu. The origin of FSu is at the center of the sensor aperture and the lenslet array of the sensor coincides with the x_1, x_2-plane of FSu. With Eq. 2 the lenslet array is tangent to the nominal sphere of the wavefront touching it at the center of the aperture.
The linearity of Eq 2 enables the following compact expression of $\boldsymbol{w}^{\{u\}}$ after inserting Eq. 1 into Eq 2

$$\boldsymbol{w}^{\{u\}} = \begin{pmatrix} \tilde{r}\, f_{u1}(\theta_1, \theta_2) \\ \tilde{r}\, f_{u2}(\theta_1, \theta_2) \\ \tilde{r}\, f_{u3}(\theta_1, \theta_2) \end{pmatrix} \approx \begin{pmatrix} r_0\, f_{u1}(\theta_1, \theta_2) \\ r_0\, f_{u2}(\theta_1, \theta_2) \\ \tilde{r}\, f_{u3}(\theta_1, \theta_2) \end{pmatrix}. \tag{3}$$

The functions f_{ui} $(i = 1..3)$ are defined by θ_{u1}, θ_{u2} and r_0. The Zernike coefficents (c_n) are only contained by $\tilde{r}$. In the third expression of Eq. 3, the first two coordinates get independent of the Zernike coefficients by replacing $\tilde{r}$ by r_0. This approximation is valid if the divergence of the wavefront segment covered by the sensor is at a scale of a few degrees.
At the lenslet array, the gradient of the wavefront is measured at the points where the wavefront hits the centers of the lenslets. The parameters of the point of the wavefront that is measured at lenslet l $(l = 1..L)$ of sensor u are denoted by $\boldsymbol{\theta}_{ul} = (\theta_1 =$

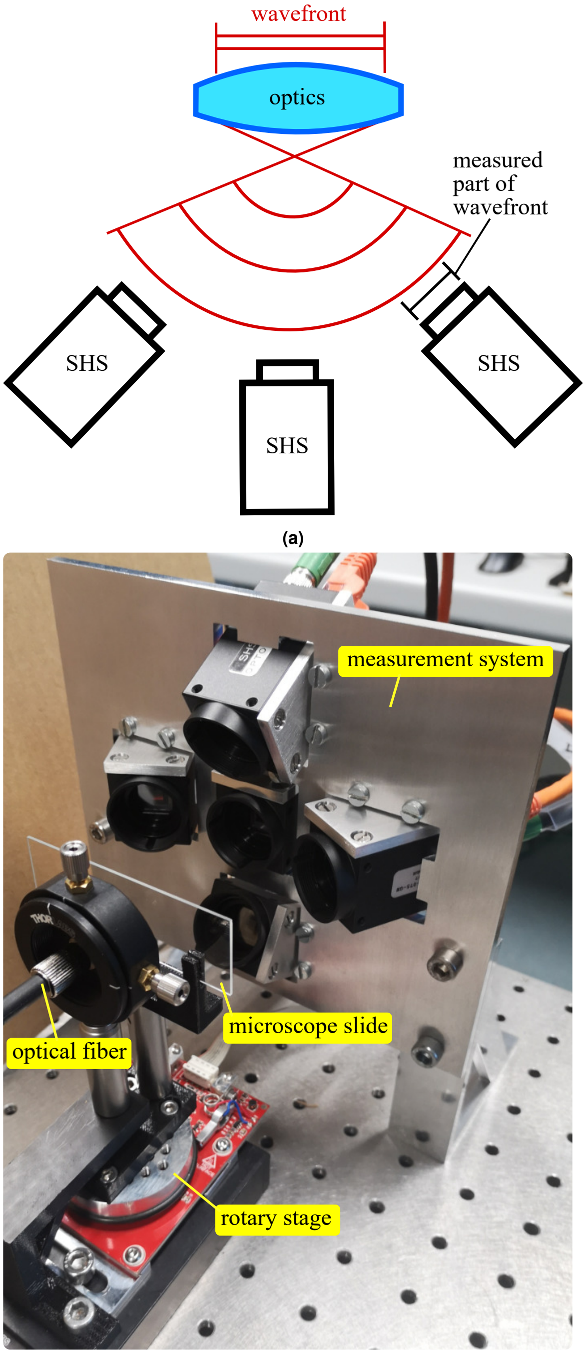

(a)

(b)

Fig. 1. (a) Measurement concept. Segments of the divergent wavefront are measured with a few SHSs. The SHS measurements can be carried out in parallel. (b) Experimental setup with five SHSs. The wavefront (divergence = 62°) originates from an optical fiber and propagates through a microscope slide to generate distortions in the wavefront.

Post-print version of the article: Nikolaus Berlakovich, Ernst Csencsics, Damian Senoner, and Georg Schitter , "Fast modal reconstruction of large plane wavefronts from sparse measurements using Shack–Hartmann sensors," *Applied Optics*, Vol. 62, Issue 26, pp. 6986-6992, 2023. DOI: 10.1364/AO.493076
© 2023 Optical Society of America. One print or electronic copy may be made for personal use only. Systematic reproduction and distribution, duplication of any material in this paper for a fee or for commercial purposes, or modifications of the content of this paper are prohibited.

Post-print version (generated on 14.12.2023)
This and other publications are available at:
http://www.acin.tuwien.ac.at/publikationen/ams/

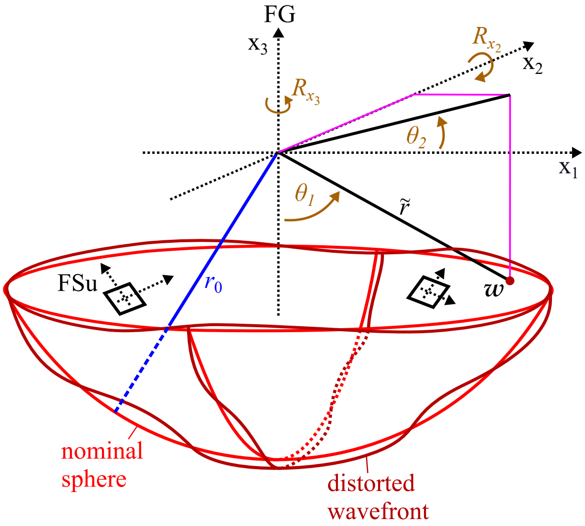

Fig. 2. Distorted wavefront parameterized $\theta_1 \in [0, \theta_{div}]$ and $\theta_2 \in [0, 2\pi]$. The point of the distorted wavefront in FG corresponding to θ_1 and θ_2 is denoted by $\boldsymbol{w}$. The radius of the nominal sphere of the wavefront is denoted by r_0.

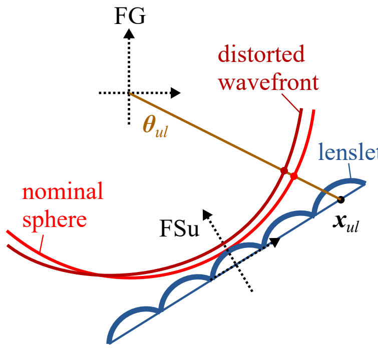

Fig. 3. The point of the wavefront with parameters $\boldsymbol{\theta}_{ul}$ is measured at lenslet position $\boldsymbol{x}_{ul}$. Neglecting the wavefront distortions leads to the computation of $\boldsymbol{\theta}_{ul}$ via the nominal sphere (see Eq. 4).

θ_{ul1}, $\theta_2 = \theta_{ul2}$) as illustrated in Fig. 3. The wavefront distortions are neglected and only the nominal sphere of the wavefront is considered for the computation of $\boldsymbol{\theta}_{ul}$. The parameters are then determined by

$$\begin{aligned} \theta_{ul1} &= arccos(-\frac{x_{ul3}}{r_0}), \\ \theta_{ul2} &= atan2(x_{ul2}, x_{ul1}), \end{aligned} \tag{4}$$

where $\boldsymbol{x}_{ul} = (x_{ul1}, x_{ul2}, x_{ul3})^T$ are the coordinates of the lenslet position in FG. With Eq. 3 and the expression for $\tilde{r}$ (see Eq. 1) the two components ($k = 1, 2$) of the gradient of the wavefront measured at lenslet position $\boldsymbol{x}_{ul}$ are then given by

$$\begin{aligned} \frac{\partial w_3^{\{u\}}}{\partial w_k^{\{u\}}}\Big|_{\boldsymbol{\theta}_{ul}} &= \sum_{m=1}^{2} \tilde{j}_{km}(\boldsymbol{\theta}_{ul}) \frac{\partial(\tilde{r} f_{u3})}{\partial \theta_m}\Big|_{\boldsymbol{\theta}_{ul}} \\ &= \sum_{m=1}^{2} r_0\, \tilde{j}_{km}(\boldsymbol{\theta}_{ul}) \frac{\partial f_{u3}}{\partial \theta_m}\Big|_{\boldsymbol{\theta}_{ul}} \\ &+ \sum_{n=1}^{N} c_n \sum_{m=1}^{2} \tilde{j}_{km}(\boldsymbol{\theta}_{ul}) \left[Z_n(\boldsymbol{\theta}_{ul}) \frac{\partial f_{u3}}{\partial \theta_m}\Big|_{\boldsymbol{\theta}_{ul}} + f_{u3}(\boldsymbol{\theta}_{ul}) \frac{\partial Z_n}{\partial \theta_m}\Big|_{\boldsymbol{\theta}_{ul}} \right] \\ &= S_{ulk} + \sum_{n=1}^{N} c_n \tilde{Z}_{nulk} \quad , \end{aligned} \tag{5}$$

with $\tilde{j}_{km}$ being an element of the transpose inverse Jacobian matrix, i.e.

$$J^{-1\,T} = \begin{pmatrix} \tilde{j}_{11} & \tilde{j}_{12} \\ \tilde{j}_{21} & \tilde{j}_{22} \end{pmatrix}, \tag{6}$$

where the expression for the Jacobian matrix is given by

$$J = \begin{pmatrix} \frac{\partial f_{u1}}{\partial \theta_1} & \frac{\partial f_{u1}}{\partial \theta_2} \\ \frac{\partial f_{u2}}{\partial \theta_1} & \frac{\partial f_{u2}}{\partial \theta_2} \end{pmatrix}. \tag{7}$$

The individual sums over m ($= 1, 2$) in the third expression of Eq. 5 are denoted by S_{ulk} and $\tilde{Z}_{nulk}$ ($n = 1..N$), where S_{ulk} corresponds to the contribution of the nominal sphere and $\tilde{Z}_{nulk}$ to the contribution of the n-th Zernike polynomial describing a specific wavefront distortion.
The measured values for the two gradient components at lenslet position $\boldsymbol{x}_{ul}$ are given by

$$g_{ulk} = \frac{\partial w_3^{\{u\}}}{\partial w_k^{\{u\}}}\Big|_{\boldsymbol{\theta}_{ul}} + \varepsilon_{ulk}^{rest} + \eta_{ulk} \quad \text{with} \quad k = 1, 2 \quad , \tag{8}$$

where η_{ulk} is the error in the measurement of the nominal sphere caused by sensor misalignment, i.e. a deviation of the sensor from its nominal position and alignment, and ε_{ulk}^{rest} is the rest of the total measurement error including noise and the rest of the error caused by sensor misalignment related to the deviation of the wavefront from the nominal sphere. η_{ulk} may be at a significantly larger scale than ε_{ulk}^{rest}, especially in the case of pitch and yaw of the sensor, and may result in large estimation errors. Measuring a spherical wavefront with the same origin as the distorted wavefront enables the measurement of the nominal sphere of the distorted wavefront leading to the following measured values at lenslet position $\boldsymbol{x}_{ul}$

$$\tilde{g}_{ulk} = S_{ulk} + \tilde{\varepsilon}_{ulk}^{rest} + \eta_{ulk} \quad \text{with} \quad k = 1, 2 \quad , \tag{9}$$

Post-print version of the article: Nikolaus Berlakovich, Ernst Csencsics, Damian Senoner, and Georg Schitter , "Fast modal reconstruction of large plane wavefronts from sparse measurements using Shack–Hartmann sensors," *Applied Optics*, Vol. 62, Issue 26, pp. 6986-6992, 2023. DOI: 10.1364/AO.493076
© 2023 Optical Society of America. One print or electronic copy may be made for personal use only. Systematic reproduction and distribution, duplication of any material in this paper for a fee or for commercial purposes, or modifications of the content of this paper are prohibited.

Post-print version (generated on 14.12.2023)
This and other publications are available at:
http://www.acin.tuwien.ac.at/publikationen/ams/

with $\tilde{\varepsilon}^{rest}_{ulk}$ being the measurement error not caused by sensor misalignment, such as noise. The difference between Eq. 8 and Eq. 9 is independent of η_{ulk} and with Eq. 5 given by

$$g_{ulk} - \tilde{g}_{ulk} = \sum_{n=1}^{N} c_n \tilde{Z}_{nulk} + \varepsilon^{rest}_{ulk} - \tilde{\varepsilon}^{rest}_{ulk} \quad . \tag{10}$$

The Zernike coefficients are then estimated with the least squares method [18] where the following expression is minimized:

$$\min_{c_1..c_N} \sum_{u,l,k} \left(g_{ulk} - \tilde{g}_{ulk} - \sum_{n=1}^{N} c_n \tilde{Z}_{nulk}\right)^2. \tag{11}$$

Transforming Eq. 11 into a matrix equation, i.e. the normal equations [19], gives

$$\boldsymbol{Q}^T \boldsymbol{Q} \boldsymbol{A} = \boldsymbol{Q}^T \boldsymbol{G}, \tag{12}$$

where $\boldsymbol{Q} \in \mathbb{R}^{(2UL)\times N}$, $\boldsymbol{A} \in \mathbb{R}^N$ and $\boldsymbol{G} \in \mathbb{R}^{2UL}$ with the following explicit expressions:

$$\boldsymbol{Q} = \begin{pmatrix} \tilde{Z}_{1111} & .. & \tilde{Z}_{N111} \\ \tilde{Z}_{1112} & .. & \tilde{Z}_{N112} \\ \vdots & & \vdots \\ \tilde{Z}_{1UL1} & .. & \tilde{Z}_{NUL1} \\ \tilde{Z}_{1UL2} & .. & \tilde{Z}_{NUL2} \end{pmatrix}, \tag{13}$$

$$\boldsymbol{A} = \begin{pmatrix} c_1 \\ \vdots \\ c_N \end{pmatrix} \quad \text{and} \quad \boldsymbol{G} = \begin{pmatrix} g_{111} - \tilde{g}_{111} \\ g_{112} - \tilde{g}_{112} \\ \vdots \\ g_{UL1} - \tilde{g}_{UL1} \\ g_{UL2} - \tilde{g}_{UL2} \end{pmatrix}. \tag{14}$$

3. SIMULATION ANALYSIS

The influence of the number of sensors, sensor misalignment, and measurement noise on the reconstruction of the wavefront is analyzed. Each of the subsequent sections is dedicated to the influence of one quantity. The quantities not analyzed in a section are equal to the corresponding values in Section A (reference settings).

A. Simulation settings

In-house software based on Matlab (The MathWorks Inc., Natick, MA, USA) in combination with OpticStudio (Zemax LLC, Kirkland, WA, USA) is used to simulate the measurement of a wavefront with a set of SHSs. Sensor misalignment as well as measurement noise are considered in the simulation. All simulated sensors are of the same model with a lenslet array consisting of 52×52 lenslets (in total 2704). Each lenslet has a pitch of $75 \times 75\,\mu m^2$ resulting in a side length of the sensor aperture of $3.9\,mm$. A wavefront with a divergence of $62°$ is simulated (see Fig. 4), where the radius of the respective nominal sphere is $90\,mm$. The distortion of the wavefront has a peak-to-valley (PV) of $13.6\,\mu m$ and contains the first 15 Zernike polynomials. The measurement of the distorted wavefront (see Eq. 8) and the measurement of a spherical wavefront (see Eq. 9) are simulated. The latter one is used to reduce the influence of sensor misalignment (see Eq. 10) which is possible if the distorted and the spherical wavefront have the same origin. The Zernike coefficients are then estimated from the measurement data using Eq. 12, where the Zernike polynomials of the first 4 orders are considered.

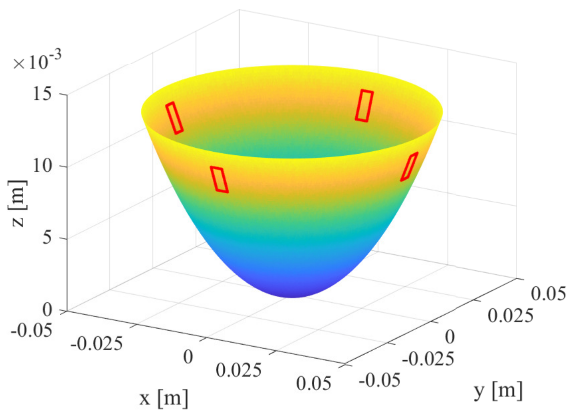

Fig. 4. Simulated distorted wavefront with a divergence of $62°$ and a nominal radius of $90\,mm$. The deviation of the wavefront from the sphere is described by a linear combination of the first 15 Zernike polynomials with a PV of $13.6\,\mu m$. The red squares correspond to the apertures of the sensors measuring segments of the wavefront.

After the estimation of the coefficients, i.e. the reconstruction of the wavefront, the difference between the reconstructed wavefront and the true wavefront is determined which corresponds to the reconstruction error. To compensate for misalignment and phase difference between the wavefronts, the true wavefront is fitted into the reconstructed wavefront [13] before calculating the difference.

In this section, 5 sensors are simulated with the following pairs of parameters defining their positions:

$$(\theta_1, \theta_2)\,[°] = (0,0),\ (28,0),\ (28,90),\ (28,180),\ (28,270). \tag{15}$$

The positions in cartesian coordinates (FG) are given by

$$\begin{pmatrix} r_0\,sin(\theta_1)\,cos(\theta_2) \\ r_0\,sin(\theta_1)\,sin(\theta_2) \\ -r_0\,cos(\theta_1) \end{pmatrix} \quad \text{with} \quad r_0 = 90\,mm. \tag{16}$$

The sensor apertures are illustrated with red squares in Fig. 4 and Fig. 5a. The SHSs are aligned in a way that their lenslet arrays are tangent to the nominal sphere of the wavefront. To simulate the expected misalignment, each sensor deviates from its nominal position and alignment [20]. The deviation from the nominal position, i.e. translational misalignment, has a standard deviation (σ) of $100\,\mu m$ with respect to each of the three spatial dimensions. Roll, pitch, and yaw of the sensor lead to a deviation from its nominal alignment, i.e. rotational misalignment, and are each simulated with a σ equal to $100\,mrad$. Measurement noise is simulated with $\sigma = 30\,\mu rad$ (angle of slope) [21]. The sensors in total measure about 1% of the wavefront, enabling the reconstruction of the wavefront (see Eq. 12) with a root mean square (RMS) value of the reconstruction error of $75\,nm$. The reconstruction error is illustrated in Fig. 5b.

Post-print version of the article: Nikolaus Berlakovich, Ernst Csencsics, Damian Senoner, and Georg Schitter , "Fast modal reconstruction of large plane wavefronts from sparse measurements using Shack–Hartmann sensors," *Applied Optics*, Vol. 62, Issue 26, pp. 6986-6992, 2023. DOI: 10.1364/AO.493076
© 2023 Optical Society of America. One print or electronic copy may be made for personal use only. Systematic reproduction and distribution, duplication of any material in this paper for a fee or for commercial purposes, or modifications of the content of this paper are prohibited.

Post-print version (generated on 14.12.2023)
This and other publications are available at:
http://www.acin.tuwien.ac.at/publikationen/ams/

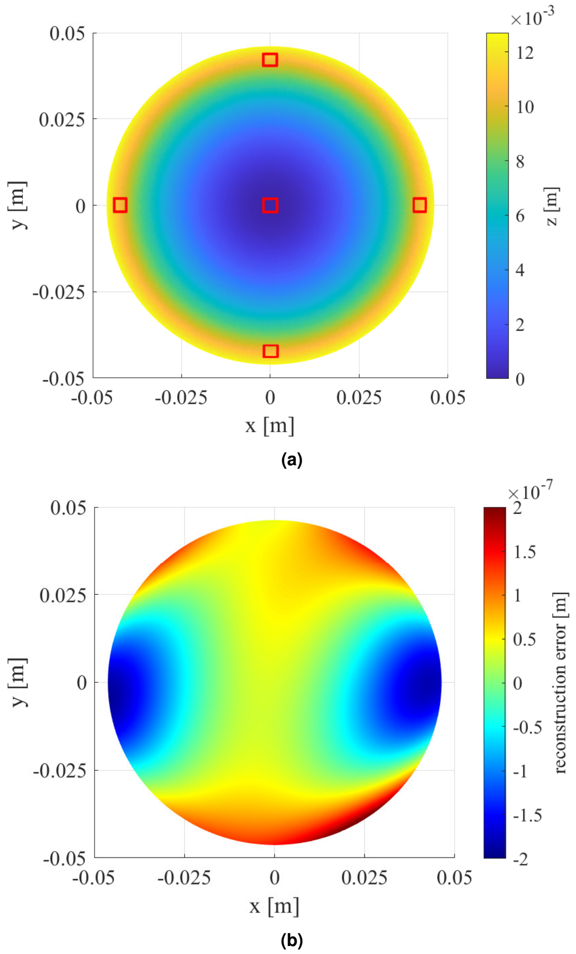

Fig. 5. (a) Sensor arrangement of the reference settings (red squares correspond to sensor apertures). (b) Reconstruction error (RMS = 75 nm) defined as the difference between the reconstructed wavefront and the true wavefront.

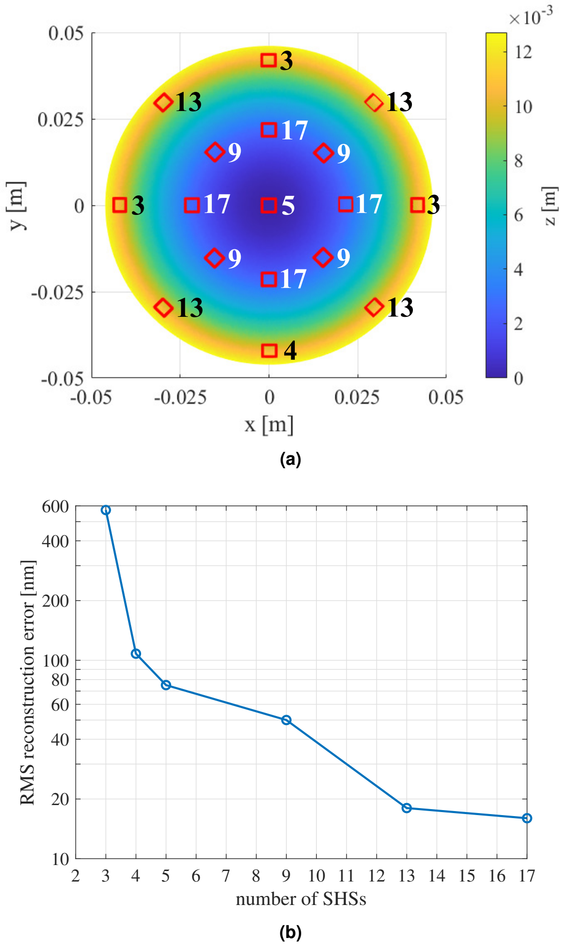

Fig. 6. (a) Sensor arrangement. Red squares correspond to sensor apertures. A sensor aperture is included in each number of sensors greater or equal to the value next to the aperture. (b) Dependence of the RMS reconstruction error (logarithmic scale) on the number of SHSs.

B. Influence of sensor number

Simulations with different numbers of sensors, i.e. 3, 4, 5, 9, 13, and 17, are carried out and the respective reconstruction error is shown in Fig. 6b. As the sensor arrangement also influences the reconstruction performance, a sensor arrangement for any number of sensors contains all sensor arrangements with lower numbers of sensors as illustrated in Fig. 6a. This enables a fair assessment of the dependence of the reconstruction error on the sensor number. A measurement with less than 4 sensors leads to large reconstruction errors beyond 500 nm. The more sensors the better the reconstruction, as the influence of measurement errors on the estimation of the Zernike coefficients decreases. With 4 sensors a reconstruction error of around 100 nm is attained, while 5 sensors result in a reconstruction error of 75 nm. For a sensor number between 5 and 13, the decrease of the reconstruction error per sensor is 7 nm on average.

C. Influence of sensor misalignment

Misalignment of the sensors is expected due to inevitable uncertainties during manufacturing and assembly. The misalignment results in a measurement error (see Eq. 8) leading to reconstruction errors. As discussed in Section A misalignment is divided into translational and rotational misalignment. Figure 7 illustrates the RMS reconstruction error vs. the standard deviation (σ) of translational misalignment of the sensors. To show the influence of rotational misalignment, two curves are illustrated for different standard deviations of rotational misalignment, i.e. $\sigma = 1\,mrad$, and $\sigma = 10\,mrad$. The values that define the simulated misalignment of a sensor are drawn from a zero-mean Gaussian distribution with the considered σ. Results show an average increase of the RMS reconstruction error by 1.3 nm if σ increases by 10 μm. The reconstruction performance hardly decreases when the rotational misalignment is increased to $\sigma = 10\,mrad$. This indicates that the influence of rotational misalignment is well reduced by subtracting the measurement

Post-print version of the article: Nikolaus Berlakovich, Ernst Csencsics, Damian Senoner, and Georg Schitter , “Fast modal reconstruction of large plane wavefronts from sparse measurements using Shack–Hartmann sensors,” *Applied Optics*, Vol. 62, Issue 26, pp. 6986-6992, 2023. DOI: 10.1364/AO.493076
© 2023 Optical Society of America. One print or electronic copy may be made for personal use only. Systematic reproduction and distribution, duplication of any material in this paper for a fee or for commercial purposes, or modifications of the content of this paper are prohibited.

Post-print version (generated on 14.12.2023)
This and other publications are available at:
http://www.acin.tuwien.ac.at/publikationen/ams/

of the spherical wavefront (see Eq. 10). In the reference settings, introduced in Section A, the origins of the distorted and the spherical wavefront coincide. However, a deviation of the origin of the spherical wavefront from the origin of the distorted wavefront may occur, as different optical systems are used to generate the wavefronts. The dependence of the RMS reconstruction error on a displacement of the spherical wavefront along the direction vector $(1,1,1)^T/\sqrt{3}$ is depicted in Fig. 8. The displacement is with respect to the origin of the distorted wavefront. The reconstruction error increases with the displacement as the calibration of the sensor misalignment with the measurement of the spherical wavefront degrades. An average decrease of the reconstruction error of 2.7 nm per 10 μm displacement of the spherical wavefront is observed.

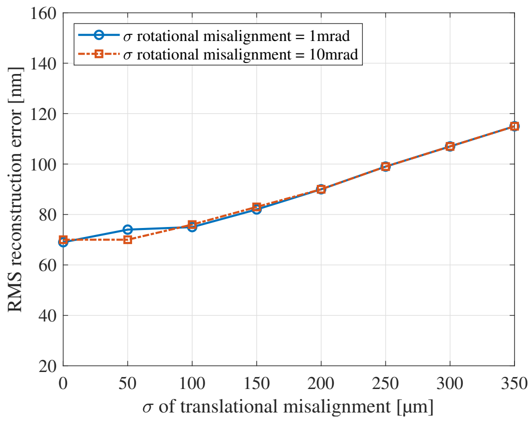

Fig. 7. Dependence of the RMS reconstruction error on σ of translational misalignment of the SHSs. One curve relates to a specific σ of rotational misalignment (i.e. 1 or 10 $mrad$).

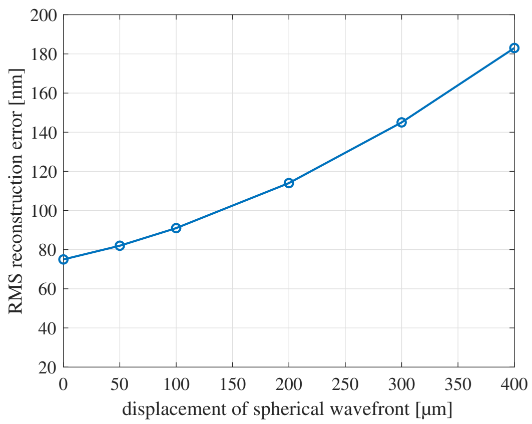

Fig. 8. Dependence of the RMS reconstruction error on the displacement of the spherical wavefront used for the calibration of sensor misalignment. The direction vector of the displacement is given by $(1,1,1)^T/\sqrt{3}$.

D. Influence of noise

Noise arising from background light, readout, or dark currents [22] is simulated by adding an error to the measurement of the gradient components (see Eq. 8). In particular, each component gets an individual error drawn from a zero-mean Gaussian distribution. Fig. 9 shows the dependence of the RMS reconstruction error on the standard deviation of noise. For a noise-free measurement ($\sigma = 0$) the reconstruction error reaches a minimum with an RMS value of 46 nm. The RMS reconstruction error increases linearly with the noise where an increase of 11.5 nm is observed if σ of noise is increased by 10 μrad.
Additionally, the measurement and reconstruction of a divergent wavefront (divergence = 62°, nominal radius = 90 mm) with a PV of 2 μm consisting of the first 15 ZP with equal coefficients (200 nm) is simulated. In Fig. 10 the estimation error of the coefficients of oblique astigmatism and of vertical astigmatism is shown in dependence of noise. The larger the gradient values of a mode at the measurement locations, the better the estimation quality of the respective coefficient, due to the higher signal-to-noise ratio (SNR). With the sensor arrangement of Fig. 5a both oblique astigmatism and vertical astigmatism provide sets of measurement data with the same SNR. Nevertheless, the coefficient error of vertical astigmatism increases significantly stronger with noise than the one of oblique astigmatism. This shows that the estimation of the coefficients is also influenced by the other modes that are assumed for the wavefront distortion.

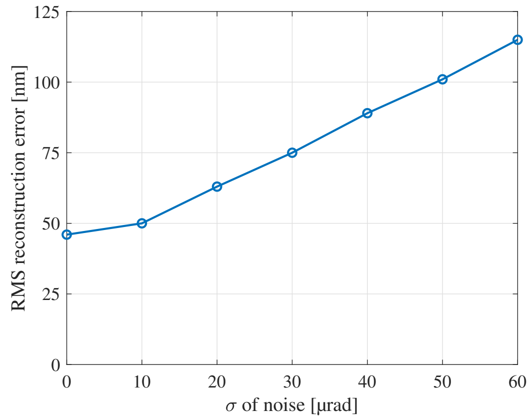

Fig. 9. Dependence of the RMS reconstruction error on σ of measurement noise.

4. EXPERIMENTAL VALIDATION OF THE CONCEPT

A spherical wavefront is generated with an optical fiber (NA = 0.5, Thorlabs Inc., Newton, NY, USA). The wavefront propagates through a microscope slide (1 mm) where it gets distorted. The corresponding setup is illustrated in Fig. 1b. The distorted wavefront with a divergence of 62° is measured with 5 commercial SHSs (AR3, Optocraft, Erlangen, Germany) at a radius of 90 mm. The sensors are mounted on an aluminum frame (see Fig. 1b) and are arranged equally to the arrangement illustrated in Fig. 5a. The sensors each have a detection area of $4.9 \times 3.7\ mm^2$ consisting of a lenslet array with 65×49 lenslets (3185 in total) with a lens-pitch of $75 \times 75\ \mu m^2$.

Post-print version of the article: Nikolaus Berlakovich, Ernst Csencsics, Damian Senoner, and Georg Schitter , "Fast modal reconstruction of large plane wavefronts from sparse measurements using Shack–Hartmann sensors," *Applied Optics*, Vol. 62, Issue 26, pp. 6986-6992, 2023. DOI: 10.1364/AO.493076
© 2023 Optical Society of America. One print or electronic copy may be made for personal use only. Systematic reproduction and distribution, duplication of any material in this paper for a fee or for commercial purposes, or modifications of the content of this paper are prohibited.

Post-print version (generated on 14.12.2023)
This and other publications are available at:
http://www.acin.tuwien.ac.at/publikationen/ams/

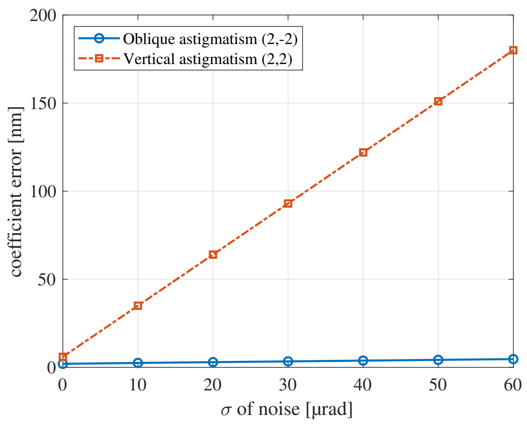

Fig. 10. Dependence of coefficient errors of oblique and vertical astigmatism on σ of measurement noise. For the sensor arrangement (Fig. 5a) both ZP lead to measured gradient values at the same scale indicating that the other ZP influences the estimation quality of the coefficients.

For the calibration of the sensor misalignment, a spherical wavefront with the same origin as the distorted wavefront is measured (see Eq. 9). The spherical wavefront is obtained by removing the microscope slide. After inserting the microscope slide, the distorted wavefront is measured and reconstructed using Eq. 12. For the reconstruction, all Zernike polynomials up to the 4th order are used and the reconstructed wavefront is shown in Fig. 11b. The reconstruction of the wavefront without the calibration of the sensor misalignment is carried out as well and shown in Fig. 11a. For this, $\boldsymbol{G}$ in Eq. 12 is replaced by $\boldsymbol{G}'$ given by

$$\boldsymbol{G}' = \begin{pmatrix} g_{111} - s_{111} \\ g_{112} - s_{112} \\ \vdots \\ g_{UL1} - s_{UL1} \\ g_{UL2} - s_{UL2} \end{pmatrix}. \quad (17)$$

Each sensor needs a measurement time of about 40 ms where 60 ms are additionally needed for the reconstruction of the wavefront on a personal computer (2.6 GHz).
Eight segments, i.e. the black rectangles in Fig. 11a and Fig. 11b, are additionally measured at other locations on the distorted wavefront of the same phase. To position the sensors to the new locations, the wavefront is rotated about the x_2-axis (see Fig. 2) by $\pm 10°$ while keeping the aluminum frame with the sensors fixed. The rotation of the wavefront is obtained by rotating the microscope slide with the rotary stage (see Fig. 1b). The segments are not used for the reconstruction of the distorted wavefront but are individually reconstructed with a state-of-the-art reconstruction algorithm [23]. Due to the dense gradient measurement of an SHS, the segments can be reconstructed with high accuracy where a reconstruction error with an RMS value of a few nanometers is attained. The segments are then fitted into the reconstructed distorted wavefront at the locations where they have been measured. The difference between the segments and the distorted wavefront is an indicator of the reconstruction quality. Omitting the calibration of the sensor misalignment leads to an insufficient reconstruction of the wavefront with an RMS value of the difference of 11 μm. A high-quality reconstruction is obtained with the calibration of the sensor misalignment where an RMS value of the differences of 11 nm is attained. The results show the importance of the calibration of the sensor misalignment and that a sufficient calibration can be obtained with the measurement of a spherical wavefront.
To obtain an estimate of the true wavefront, the setup (with the microscope slide) for generating the wavefront (Fig. 1b) is simulated and the wavefront is determined via raytracing. Subtracting the nominal sphere from the simulated and the reconstructed wavefront leads to the simulated and measured wavefront distortion, respectively, depicted in Fig. 12. As expected, the distortion is similar to the spherical aberration [16]. The RMS difference between the simulated and the reconstructed wavefront is 200 nm which is an estimate for the true RMS reconstruction error. However, the true reconstruction error may be smaller, as in the simulation the nominal dimensions and material properties of the setup are considered which may deviate from the actual dimensions and material properties.

In summary, the successful reconstruction of a highly divergent wavefront (62°) from sparse SHS measurements is demonstrated. Results show that the wavefront can be reconstructed with a reconstruction error at the scale of 75 nm from a measurement of 1 % of the wavefront.

5. CONCLUSIONS

This contribution presents a concept for the sparse measurement and reconstruction of a highly divergent wavefront. The concept enables a direct measurement of the wavefront meaning that no supporting optics are needed for reshaping the wavefront before the measurement. A measurement system using SHSs is proposed and the mathematics enabling a successful reconstruction of the wavefront are discussed. For the evaluation of the concept with respect to measurement errors, caused by sensor misalignment and noise, a simulation analysis is presented. Results show that a measurement of 1 % of a wavefront with a divergence of 62° can be sufficient for a successful reconstruction of the wavefront with an error at the scale of 75 nm. The concept is experimentally validated with a measurement system consisting of 5 SHSs showing a reconstruction error of 200 nm. The sparse measurement results in low measurement times making the concept suitable for the inline measurement of optical systems.

Acknowledgement. We thank Ulrich Berg from Optocraft GmbH for his support and fruitful discussions.

Disclosures. The authors declare no conflicts of interest.

Data availability. Data underlying the results presented in this paper are not publicly available at this time but may be obtained from the authors upon reasonable request.

REFERENCES

1. C. Vérinaud, M. Le Louarn, V. Korkiakoski, and M. Carbillet, "Adaptive optics for high-contrast imaging: pyramid sensor versus spatially filtered shack—hartmann sensor," Mon. Notices Royal Astron. Soc. Lett. **357**, L26–L30 (2005).

Post-print version of the article: Nikolaus Berlakovich, Ernst Csencsics, Damian Senoner, and Georg Schitter , "Fast modal reconstruction of large plane wavefronts from sparse measurements using Shack–Hartmann sensors," *Applied Optics*, Vol. 62, Issue 26, pp. 6986-6992, 2023. DOI: 10.1364/AO.493076
© 2023 Optical Society of America. One print or electronic copy may be made for personal use only. Systematic reproduction and distribution, duplication of any material in this paper for a fee or for commercial purposes, or modifications of the content of this paper are prohibited.

Post-print version (generated on 14.12.2023)
This and other publications are available at:
http://www.acin.tuwien.ac.at/publikationen/ams/

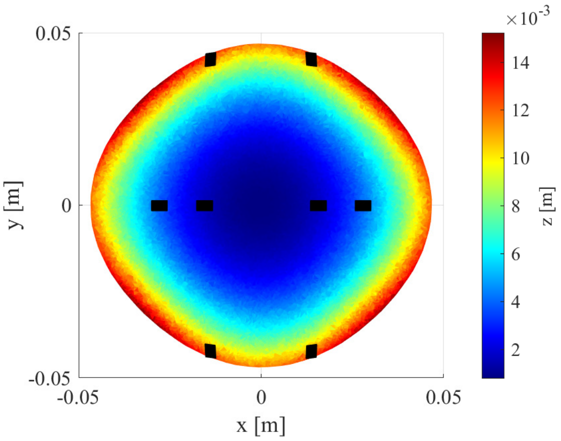

(a) misalignment calibration off
RMS difference = 11 μm

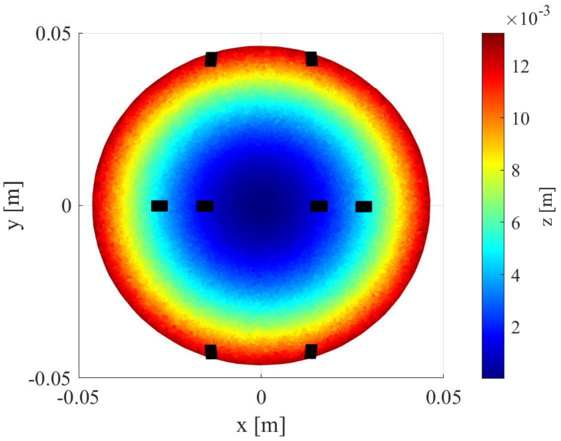

(b) misalignment calibration on
RMS difference = 11 nm

Fig. 11. Eight segments (black rectangles) are additionally measured at further locations on the wavefront. The segments are not used for the reconstruction of the wavefront and are fitted into the reconstructed wavefront where the difference between the segments and the wavefront is a measure of the reconstruction accuracy.

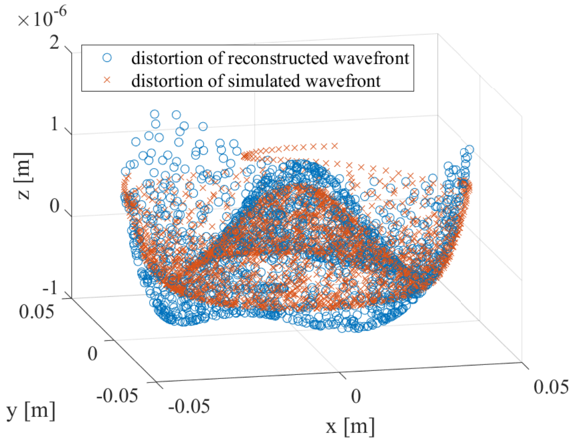

Fig. 12. Distortion of the reconstructed (blue circles) and the simulated wavefront (orange crosses), with respect to the nominal spherical wavefront. The spherical aberration is the dominating mode. The RMS difference between the reconstructed and the simulated wavefront is 200 nm.

2. F. Rigaut, "Astronomical adaptive optics," Publ. Astron. Soc. Pac. **127**, 1197–1203 (2015).
3. J. Liang, B. Grimm, S. Goelz, and J. F. Bille, "Objective measurement of wave aberrations of the human eye with the use of a hartmann–shack wave-front sensor," JOSA A **11**, 1949–1957 (1994).
4. R. K. Tyson, *Adaptive optics engineering handbook* (Marcel Dekker New York, 2000).
5. J. Sheldakova, A. Kudryashov, V. Zavalova, and P. Romanov, "Shack-hartmann wavefront sensor versus fizeau interferometer for laser beam measurements," in *Laser Resonators and Beam Control XI,* vol. 7194 (International Society for Optics and Photonics, 2009), p. 71940B.
6. M. Rocktäschel and H. Tiziani, "Limitations of the shack–hartmann sensor for testing optical aspherics," Opt. & Laser Technol. **34**, 631–637 (2002).
7. D. R. Burada, K. K. Pant, M. Bichra, G. S. Khan, S. Sinzinger, and C. Shakher, "Experimental investigations on characterization of freeform wavefront using shack–hartmann sensor," Opt. Eng. **56**, 084107 (2017).
8. M. E. Fuerst and G. Schitter, "Scanning wavefront sensor for measurement of highly divergent wavefronts," IFAC-PapersOnLine. **52**, 25–30 (2019).
9. M. E. Fuerst, E. Csencsics, N. Berlakovich, and G. Schitter, "Automated measurement of highly divergent optical wavefronts with a scanning shack–hartmann sensor," IEEE Transactions on Instrumentation Meas. **70**, 1–9 (2020).
10. N. Berlakovich, M. E. Fuerst, E. Csencsics, and G. Schitter, "Robust wavefront segment registration based on a parallel approach," Appl. Opt. **60**, 1578–1586 (2021).
11. N. Berlakovich, E. Csencsics, M. Fuerst, and G. Schitter, "Fast, precise, and shape-flexible registration of wavefronts," Appl. Opt. **60**, 6781–6790 (2021).
12. N. Berlakovich, E. Csencsics, M. Fuerst, and G. Schitter, "Iterative parallel registration of strongly misaligned wavefront segments," Opt. Express **29**, 33281–33296 (2021).
13. N. Berlakovich, M. Fuerst, E. Csencsics, and G. Schitter, "Improving the precision of parallel registration by incorporating a priori information," Opt. Express **30**, 41473–41491 (2022).
14. S. Chen, S. Li, and Y. Dai, "Iterative algorithm for subaperture stitching interferometry for general surfaces," JOSA A **22**, 1929–1936 (2005).
15. N. Berlakovich, E. Csencsics, D. Senoner, and G. Schitter, "Fast modal reconstruction of large plane wavefronts from sparse measurements using shack-hartmann sensors[manuscript submitted for publication]," Appl. Opt. (2023).
16. V. Lakshminarayanan and A. Fleck, "Zernike polynomials: a guide," J. Mod. Opt. **58**, 545–561 (2011).
17. S. McKnight and C. Zahopoulos, *Scientific Foundations of Engineering* (Cambridge University Press, 2015).
18. S. J. Miller, "The method of least squares," Math. Dep. Brown Univ. **8**, 1–7 (2006).
19. J. Blais, "Least squares for practitioners," Math. Probl. Eng. **2010** (2010).
20. J. Ma, D. Lu, and W. Zhao, "Assembly errors analysis of linear axis of cnc machine tool considering component deformation," The Int. J. Adv. Manuf. Technol. **86**, 281–289 (2016).
21. D. R. Neal, J. Copland, and D. A. Neal, "Shack-hartmann wavefront sensor precision and accuracy," in *Advanced Characterization Techniques for Optical, Semiconductor, and Data Storage Components,* vol. 4779 (International Society for Optics and Photonics, 2002), pp.

Post-print version of the article: Nikolaus Berlakovich, Ernst Csencsics, Damian Senoner, and Georg Schitter , "Fast modal reconstruction of large plane wavefronts from sparse measurements using Shack–Hartmann sensors," *Applied Optics*, Vol. 62, Issue 26, pp. 6986-6992, 2023. DOI: 10.1364/AO.493076
© 2023 Optical Society of America. One print or electronic copy may be made for personal use only. Systematic reproduction and distribution, duplication of any material in this paper for a fee or for commercial purposes, or modifications of the content of this paper are prohibited.

Post-print version (generated on 14.12.2023)
This and other publications are available at:
http://www.acin.tuwien.ac.at/publikationen/ams/

148–160.

22. H. Mao, Y. Liang, J. Liu, and Z. Huang, "A noise error estimation method for shack-hartmann wavefront sensor," in *AOPC 2015: Telescope and Space Optical Instrumentation,* vol. 9678 (International Society for Optics and Photonics, 2015), p. 967811.
23. L. Huang, J. Xue, B. Gao, C. Zuo, and M. Idir, "Spline based least squares integration for two-dimensional shape or wavefront reconstruction," Opt. Lasers Eng. **91**, 221–226 (2017).

Post-print version of the article: Nikolaus Berlakovich, Ernst Csencsics, Damian Senoner, and Georg Schitter , "Fast modal reconstruction of large plane wavefronts from sparse measurements using Shack–Hartmann sensors," *Applied Optics*, Vol. 62, Issue 26, pp. 6986-6992, 2023. DOI: 10.1364/AO.493076
© 2023 Optical Society of America. One print or electronic copy may be made for personal use only. Systematic reproduction and distribution, duplication of any material in this paper for a fee or for commercial purposes, or modifications of the content of this paper are prohibited.